Available online at www.sciencedirect.com
ScienceDirect
Trans. Nonferrous Met. Soc. China 34(2024) 3504−3520
Transactions of Nonferrous Metals Society of China
www.tnmsc.cn

Hybrid machine learning and microstructure-based approach for modeling relationship between microstructure and hardness of AA2099 Al−Li alloy

Xiang-hui ZHU[1,2#], Xu-sheng YANG[2#], Wei-jiu HUANG[1,2], Miao GONG[3], Xin WANG[1], Meng-di LI[4]

1. Faculty of Materials Science and Engineering, Kunming University of Science and Technology, Kunming 650093, China;
2. College of Materials Science and Engineering, Chongqing University of Arts and Sciences, Chongqing 402160, China;
3. College of Materials Science and Engineering, Chongqing University of Technology, Chongqing 400044, China;
4. College of Materials Science and Engineering, Chongqing University, Chongqing 400044, China

Received 18 July 2023; accepted 4 March 2024

Abstract: A hybrid approach combining machine learning and microstructure analysis was proposed to investigate the relationship between microstructure and hardness of AA2099 Al−Li alloy through nano-indentation, X-ray diffraction (XRD) and electron backscatter diffraction (EBSD) technologies. Random forest regression (RFR) model was employed to predict hardness based on microstructural features and uncover influential factors and their rankings. The results show that the increased hardness correlates with a smaller distance from indentation to grain boundary (D_{dis}) or a shorter minimum grain axis (D_{min}), a lower Schmidt factor in friction stir weld direction (SF_{FD}), and higher sine values of the angle between {111} slip plane and surface (sin θ_{min}). D_{dis} and D_{min} emerge as pivotal determinants in hardness prediction. High-angle grain boundaries imped dislocation slip, thereby increasing hardness. Crystallographic orientation also significantly influences hardness, especially in the presence of T_1 phases along $\{111\}_{Al}$ habit planes. This effect is attributable to the variation in encountered T_1 variants during indenter loading. Consequently, the importance ranking of microstructural features shifts depending on T_1 phase abundance: in samples with limited T_1 phases, D_{dis} or D_{min} > SF_{FD} > sin θ_{min}, while in samples with abundant T_1 phases, D_{dis} or D_{min} > sin θ_{min} > SF_{FD}.
Key words: machine learning; T_1 phase; hardness; Al−Li alloy

1 Introduction

Understanding the relationship between the microstructure and mechanical properties of alloys is critically important in the field of materials science and engineering [1−4]. By manipulating composition, processing methods, and heat treatments, it becomes feasible to control the microstructural features and, ultimately, to tailor the mechanical performance of the material [5−7]. For instance, precise control of the grain size and orientation can enhance the strength and ductility of alloys. Similarly, optimizing phase distribution allows for improvements in the corrosion resistance, hardness, and other critical mechanical performance [8−10].

In recent decades, significant progress has been made in understanding relationship between the microstructure and mechanical properties, and

# Xiang-hui ZHU and Xu-sheng YANG contributed equally to this work
Corresponding author: Wei-jiu HUANG, Tel: +86-23-49891900, E-mail: huangweijiu@cqut.edu.cn
DOI: 10.1016/S1003-6326(24)66622-7

quantitatively predicting the individual strengthening effect in alloys [11−13]. While advanced experimental and computational techniques are available for characterizing the microstructure of alloys [14,15], challenges persist in dealing with complex alloy systems. There are numerous interactions and coupling effects between alloy microstructure and mechanical properties [16]. The burgeoning field of machine learning-driven research on material performance provides new insights for addressing this issue [17−19]. By collecting appropriate training feature parameter data and utilizing machine learning methods, researchers can develop correlation models that link the feature parameters of alloys with their performance. Machine learning methods are capable of predicting an alloy's mechanical performance and of ranking the importance of microstructural features [20]. This, in turn, guides the development of mathematical and physical models, deepening our understanding of the microstructure−property relationship in alloys [21], which is crucial for optimizing mechanical performance.

Fundamentally, most machine learning algorithms are founded on the premise that more data improve predictive or classification performance [17]. In many practical applications, larger datasets enable these models to discern finer nuances, understand complex relationships and obscure trends within the data. However, obtaining large volumes of high-quality data can be a challenge, especially when dealing with specialized domains or instances where data collection is expensive or time-consuming, such as predicting the mechanical performance of alloys. Nano-indentation has emerged as a standard, high-throughput experimental method for studying the mechanical behavior and characterizing the mechanical properties of various materials on a minuscule scale [22,23]. This high-throughput experimentation approach facilitates the exploration of an extensive array of conditions or combinations, resulting in the production of rich datasets.

In this work, we aimed at investigating the relationship between the microstructure and hardness of AA2099 Al−Li alloy. A dataset capturing the microstructural features and corresponding hardness values was established utilizing hardness testing and a range of techniques for microstructural characterization. The underlying mechanism connecting the microstructural characteristics to the hardness of AA2099 Al−Li alloy was unveiled through the integration of machine learning data mining and slip trace analysis. Furthermore, a novel hybrid machine learning and microstructure-based approach for modeling the microstructure−hardness relationship of the AA2099 Al−Li alloy was proposed to better understand this important material system.

2 Methods

2.1 Experimental details

AA2099 Al−Li alloy (Cu 2.78 wt.%; Li 1.80 wt.%; Zn 0.67 wt.%; Mg 0.30 wt.%; Mn 0.36 wt.%; Zr 0.09 wt.%; Fe 0.03 wt.%; Al balanced) was employed in this study. To achieve the targeted grain size, the plates underwent stir friction welding. The samples were prepared through different heat treatments. Each test sample was solution-treated at 540 °C and water-quenched, followed by a natural aging step of several weeks at room temperature (named as T4). Subsequently, a subset of these samples were subjected to artificial aging at 160 °C for 24 h (named as T6). Other samples were pre-deformed to strains of 3% and 6% (named as T3-3% and T3-6%, respectively), and then artificial aged immediately at 160 °C for 24 h (named as T8-3% and T8-6%, respectively).

For nanoindentation tests, samples measuring 10 mm × 15 mm × 5 mm were extracted from the plates subjected to stir friction welding, as shown in Fig. 1. The tests were performed using an Agilent G200 nano-indenter with a trihedral Berkovich indenter at a constant strain rate of 0.05 s^{-1}. The tests applied the continuous stiffness measurement mode with a maximum penetration depth of 2 μm. Samples for the nanoindentation tests were prepared through grinding and electrochemically polishing in a mixed solution of 10 mL $HClO_4$ and 90 mL ethanol at 20 V and −25 °C. After the nanoindentation tests, the samples were subjected to electron backscatter diffraction (EBSD) investigation using a Zeiss Gemini 300 field emission gun scanning electron microscope (SEM) with an Oxford Symmetry S1 detector.

For transmission electron microscopy (TEM) observations, the samples were carefully ground to the thickness of 70 μm. These were then formed into

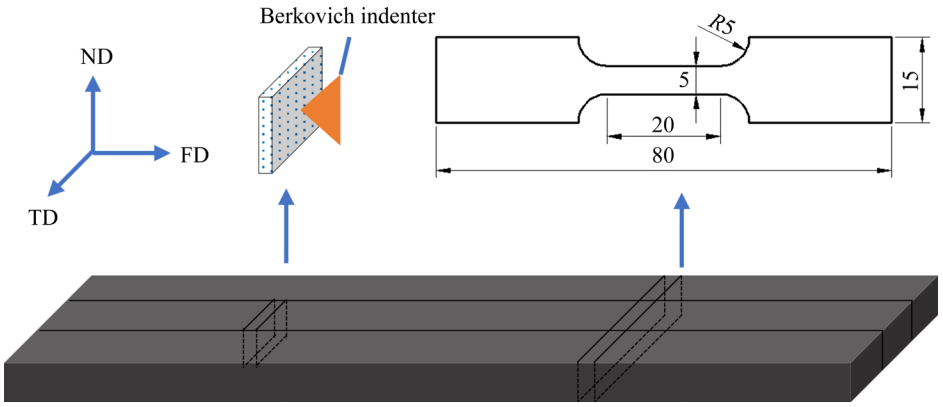

Fig. 1 Schematic diagrams showing coordinate system and test samples (Unit: mm)

3 mm diameter disks, which were electropolished using a twin-jet electro- polishing instrument in a 33 vol.% nitric acid methanol solution for 40 s at −30 °C under 15 V. The observations were carried out with an FEI Talos F200X operated at 200 kV utilizing bright field (BF), high-angle annular dark field (HAADF) and selected area electron diffraction (SAED).

Dislocation density was measured using X-ray diffraction (XRD) line profile analysis. A Bruker D8 Advance instrument was used with Cu K_α radiation. The instrument settings were adjusted to a twin primary of 1 mm and a secondary twin of 5 mm over a scanning range 2θ of 35°−140° at a scanning speed of 0.05 (°)/s.

Pre-deforming and tensile testing were carried out on a WANCE electro-hydraulic servo testing machine at a strain rate of $8\times10^{-4}\ s^{-1}$. The clip extensometer gauge length was 12.5 mm. All samples were machined along the rolling direction with a cross-section of 5 mm × 2 mm and a gauge length of 20 mm, as shown in Fig. 1. The final mechanical property data were the average value of three tensile samples. The yield strength of the annealed AA2099 Al−Li alloy, tested immediately after solution treatment, was determined to be 153.30 MPa.

2.2 Database generation

Data collection is a crucial aspect of machine learning, providing relevant datasets and features for analysis [24]. This study focused specifically on acquiring data related to hardness and microstructure characteristic parameters. Hardness data were obtained via nanoindentation tests. Concurrently, the microstructure characteristic parameters corresponding to the hardness indentations were identified as independent variable features as they provide valuable insights into the microstructural properties of the material. For each sample, 12 relevant features were carefully selected to capture important aspects of the microstructure. To gather necessary data for feature extraction, EBSD data were utilized. From the EBSD data, crystallographic and geometric features relevant to the study were extracted, forming the feature dataset.

A critical aspect of our data collection process was to ensure an adequate representation of the microstructural characteristics. This was achieved by having each sample group at least 250 points. Including a sufficient number of data points allowed the dataset to capture the diverse microstructural characteristics present in the samples.

The meticulous data collection process yielded a feature database containing approximately 1200 data points, each with 12 features. The database served as a comprehensive resource for subsequent machine learning analysis, facilitating the exploration of relationships between the independent variable features and the dependent variable dataset of hardness data.

2.3 Developing microstructural descriptors

The feature engineering was meticulously executed, using knowledge of the pertaining field to develop a set of features for the machine learning algorithm. This process was guided by understanding that the plastic deformation behavior of a material is strongly correlated with its microstructure and the loading conditions. For hardness prediction, both crystallographic and geometric

microstructural descriptors formed the professional knowledge-based feature set.

2.3.1 Crystallographic descriptors

Under specific loading conditions, the flow stress is determined by the grain orientation, which can be captured by Euler angles. However, it is difficult to interpret hardness results directly from Euler angles due to the non-linearity of Euler space. Hence, the following features were developed to better represent the grain crystallographic properties.

(1) Schmidt factor

During the plastic deformation process of alloys, the Schmidt factor plays a crucial role in determining how easily a crystal lattice slips along its slip plane. Schmidt factors for the applied stress along friction stir weld direction (FD), transverse direction (TD), and normal direction (ND) were named as SF_{FD}, SF_{TD}, and SF_{ND}, respectively. The average Schmidt factor across these three directions is named as SF_{avg}.

(2) Sine/cosine value of angle between {111} slip plane and surface plane

When the sine or cosine value of the angle between the slip plane and the surface plane (TD−ND plane) changes, different slip systems are activated, leading to variations in the Schmidt factors. Additionally, the presence of {111} habit planes for the T_1 phase, which has a high aspect ratio, may result in differences in the loading resistance between the inclined T_1 phase and the edge-on T_1 phase. To quantify these angles, the sine and cosine values of the minimum angle between the {111} slip plane and the surface are named as $\sin\theta_{min}$ and $\cos\theta_{min}$, respectively. The sine and cosine values of the maximum angle between the {111} slip plane and the surface are named as $\sin\theta_{max}$ and $\cos\theta_{max}$, respectively. The sine and cosine values of the average angle between the {111} slip plane and the surface are named $\sin\theta_{avg}$ and $\cos\theta_{avg}$, respectively.

2.3.2 Geometrical descriptors

Grain boundaries are important microstructural features that affect the mechanical performance of metal materials. When these materials undergo deformation process, mobile dislocations pile up at grain boundaries, causing stress concentration. A key aspect of grain boundaries is their relationship to grain size: the smaller the grain size, the higher the total grain boundary surface area per unit volume, which means that the material can withstand higher loads. Therefore, the distance from each hardness point to the nearest grain boundary (D_{dis}) and the minimum axis of the grain (D_{min}) are selected as geometric features for predicting nanoindentation hardness.

2.4 Machine learning methods

Machine learning is a statistical framework that automates analytical model fitting for data analysis such as finding structure in data (clustering) and making data-driven predictions or decisions. In this study, predicting hardness involves a binary classification problem. Machine learning methods can effectively uncover relationships between the microstructural descriptors (represented as features) and the micromechanical outcome of interest.

During data collection, it is important to account for potential outliers that may arise due to statistical errors, sample organization defects, or other factors. To manage this, a clustering algorithm was employed to cluster all samples in the dataset, followed by an analysis to determine the degree of isolation for each sample point based on the clustering information. A threshold for the degree of belonging was set to pinpoint a specified number of isolated points. Furthermore, the initial distribution of data features was analyzed to detect and exclude abnormal or noisy data points. This step involves identifying data points with exceptional degree more than 3 using isolated point analysis and subsequently removing outlier data points using the quartile range method.

The primary objective of this research is to comprehend the microstructural attributes that influence hardness. To this end, we employed a transparent machine learning approach known as random forest regression (RFR) algorithm [25]. RFR transparently selects features and builds models, ensuring that they represent the training data and generalize well to unseen data. This enhances the accuracy of the model and the reliability of the prediction results by eliminating irrelevant or redundant parameters.

Model hyperparameters consist of the number of decision trees, the number of features, and the depth of each decision tree. These hyperparameters were carefully chosen and optimized by the iterative adjustment process. The optimized values determined through the optimization process were maximum depth of 30 and estimators number of 2.

A robust data-driven model should perform well on the training data and generalize effectively on test data. We divided our dataset into two parts: 70% for training to conduct preliminary regression analysis, and the remaining 30% for testing to assess the performance of the machine learning models. To evaluate the prediction results, the R^2 (coefficient of determination) value was used.

The iterative process of the model involves several steps aimed at improving its performance. One of these steps includes increasing the volume of data samples, which helps to enhance the model's training and generalization capabilities. Additionally, modifying and fine-tuning the model parameters is another crucial aspect of the iterative process. By carefully adjusting these parameters, the model can better adapt to the specific task at hand, optimizing its accuracy and effectiveness. Overall, through these iterative steps, the model continuously evolves and improves its capabilities to deliver reliable and accurate results.

3 Results

3.1 Microstructure characteristics under different heat treatments

3.1.1 Grain structures and precipitation characteristics

Figure 2 shows the inverse pole figure (IPF) maps with grain boundaries of AA2099 Al−Li alloy under different processing conditions. After solution treatment, all samples are predominantly composed of recrystallized grains. The IPF maps on the ND−TD plane exhibit a mostly recrystallized microstructure with elongated grains dominated by fiber textures ⟨111⟩//TD.

Figure 3 shows HAADF images of the precipitates and the corresponding SAED maps of the samples under various aging conditions. Due to the absence of artificial aging, the occurrence of precipitate phases is scarcely observed in the T4 sample (Fig. 3(a)). Without pre-straining, as depicted in Fig. 3(b), a high density of small plates is present on the {100} matrix planes with a small amount of T_1 present on the {111} matrix planes in the T6 sample. Figures 3(e, f) show a high-resolution TEM image of the small plates and the corresponding fast Fourier transform (FFT) image, where the plates with a bright Cu layer are Cu-rich zones (GP I) [26]. Due to the introduction of a significant number of nucleation sites through pre-straining [4], the T8-3% and T8-6% samples precipitate more uniform T_1 phase with a small content of GP I, as shown in Figs. 3(c, d). The results demonstrate a corresponding increment in the number density and a decrement in average diameter of the T_1 phase with rising the pre-strain.

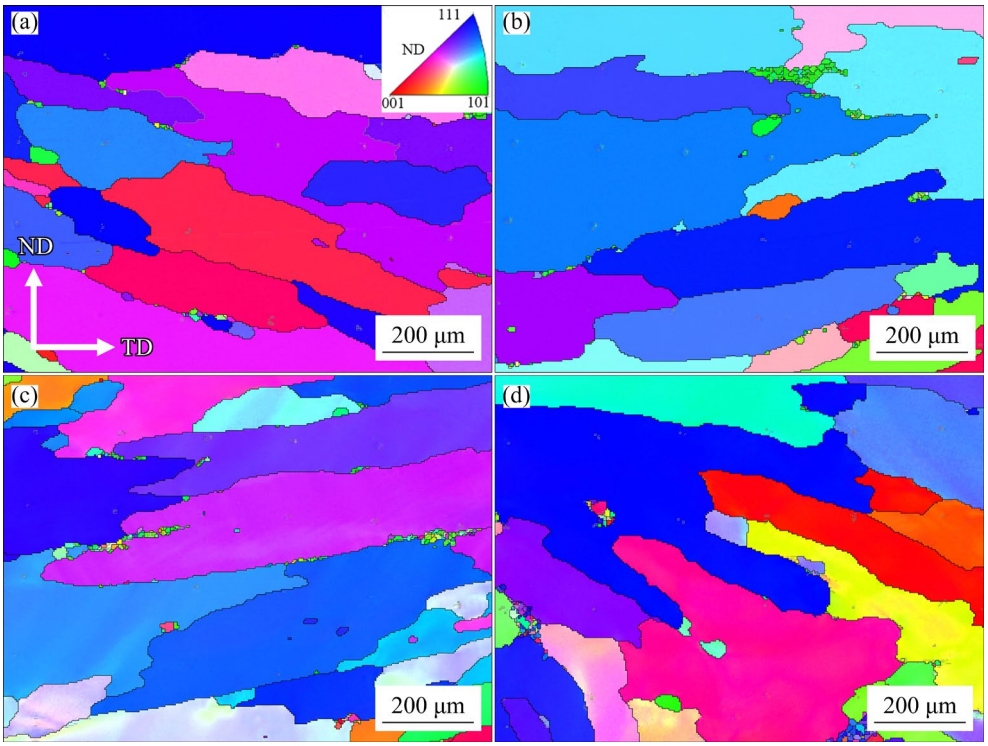

Fig. 2 IPF maps of tested samples: (a) T4; (b) T6; (c) T8-3%; (d) T8-6%

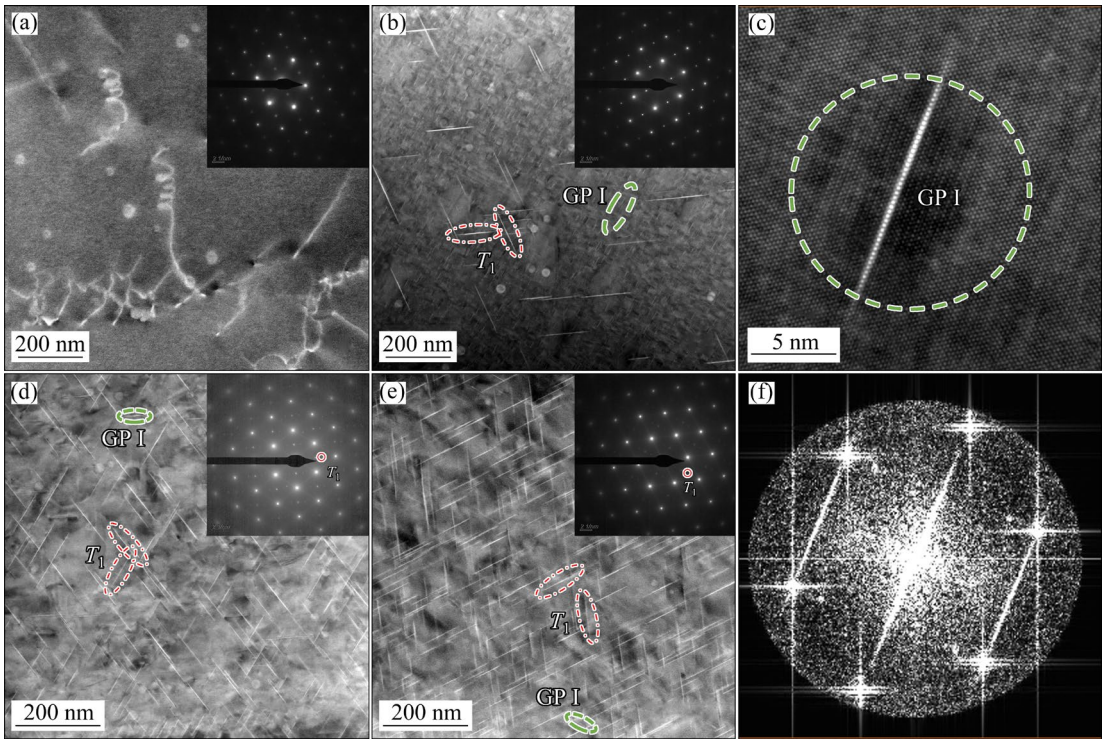

Fig. 3 HAADF images along $\langle 110 \rangle_{Al}$ zone axis of samples and corresponding SAED maps: (a) T4; (b) T6; (c) T8-3%; (d) T8-6%; (e) High-resolution TEM image of small plates present on {100} matrix planes; (f) Corresponding FFT image in (e)

3.1.2 Dislocation structures

The TEM bright field images in Fig. 4 show the dislocation structures in AA2099 Al−Li alloy under different heat treatments. It can be observed that a small number of dislocations are present in the T4 and T6 samples, whereas the T8-3% and T8-6% samples exhibit a uniform and high density of dislocations after pre-stretching.

The high dislocation density presented in Fig. 4 poses challenges for precise measurement. To supplement qualitative TEM observations, XRD peak broadening analysis was conducted for the T3-3% and T3-6% samples. Diffraction peak broadening is related to dislocation density and nanocrystalline structures [27−29]. However, in this study, owing to the large grain size (>10 μm), the observed peak broadening can be attributed to the presence of high dislocation density.

The XRD peak profiles of the {200}, {220}, {311} and {420} planes under different heat treatments were measured to analyze the effect of dislocation density on peak broadening. A Pseudo-Voigt distribution function was employed to fit each diffraction peak, allowing for the estimation of the full width at half-maximum (FWHM). Subsequently, the dislocation density values were calculated utilizing the modified Williamson−Hall model [30,31]:

$$\Delta K = 0.9/D + (\pi A^2 b^2/2)^{1/2} \rho^{1/2} K\overline{C}^{1/2} \quad (1)$$

where ΔK is the strain broadened FWHM in reciprocal space given by

$$\Delta K = 2\cos\theta \cdot \Delta\theta/\lambda \quad (2)$$

where θ is the diffraction angle, $\Delta\theta$ is the FWHM, λ is the wavelength of the X-ray (0.15418 nm for Cu radiation), and K is the amplitude of the diffraction vector defined by

$$K = 2\sin\theta/\lambda \quad (3)$$

D, ρ and b represent the average grain size, the dislocation density and the magnitude of the Burgers vector (0.286 nm for Al), respectively. A is the Wilkens arrangement parameter (0.63 for this work) [30]. $\overline{C}$ is the average contrast factor for different diffraction peaks. The software package ANIZC was utilized to calculate the required average contrast factors [32]. As a result, ΔK is modified and fitted among the (hkl) reflections as a function of $K\overline{C}^{1/2}$, as shown in Fig. 5(a). The effective dislocation densities calculated by this

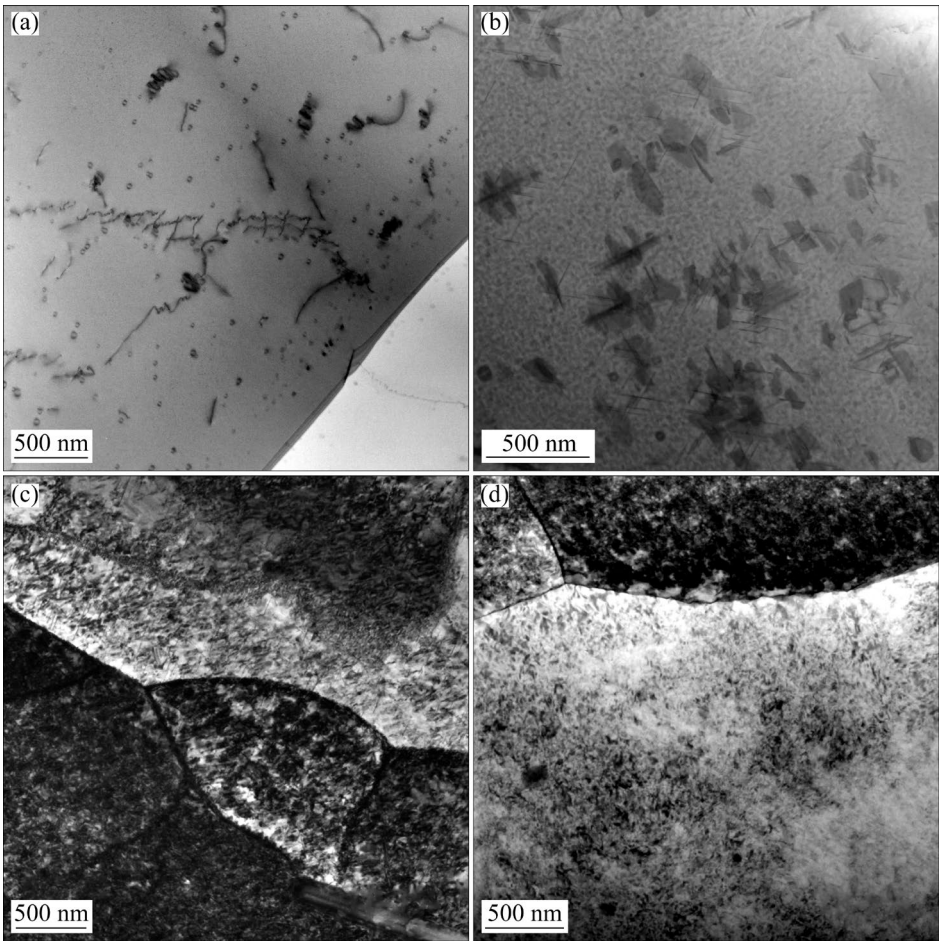

Fig. 4 Bright field TEM images showing dislocation structures in AA2099 Al−Li alloy under different heat treatments: (a) T4; (b) T6; (c) T8-3%; (d) T8-6%

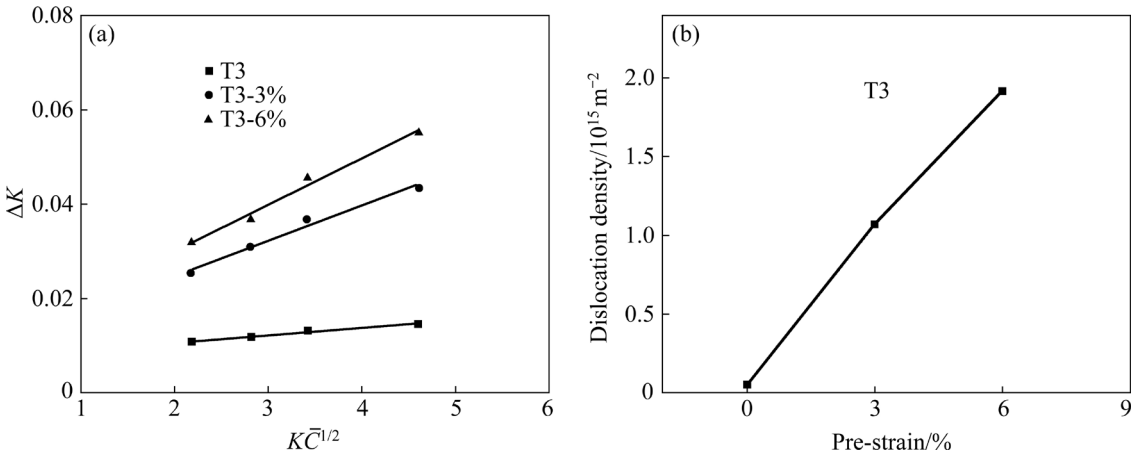

Fig. 5 Peak broadening analysis results (a) and effective dislocation density (b) obtained by modified Williamson−Hall method

method were plotted against the level of pre-strain for the T3 sample in Fig. 5(b). The results reveal a near-linear increment in dislocation density with rising pre-strain levels. Due to strong solute interaction between dislocations and solute atoms, the recovery of dislocations in the aging stage is greatly inhibited [27]. Therefore, the strength increment of dislocation strengthening induced by pre-strain is considered to remain unchanged in the T8 samples.

3.2 Hardness and tensile strength under different heat treatments

Figure 6(a) presents the hardness−displacement curves for different samples. Notably, a significant size effect is observed in hardness, whereby the hardness progressively decreases with an increase in indentation depth. This decrease stabilizes upon reaching a depth of 1 μm. Consequently, the average hardness values, measured within the depth range of 1−1.1 μm, were utilized to compare the hardness of different indentation points among different samples.

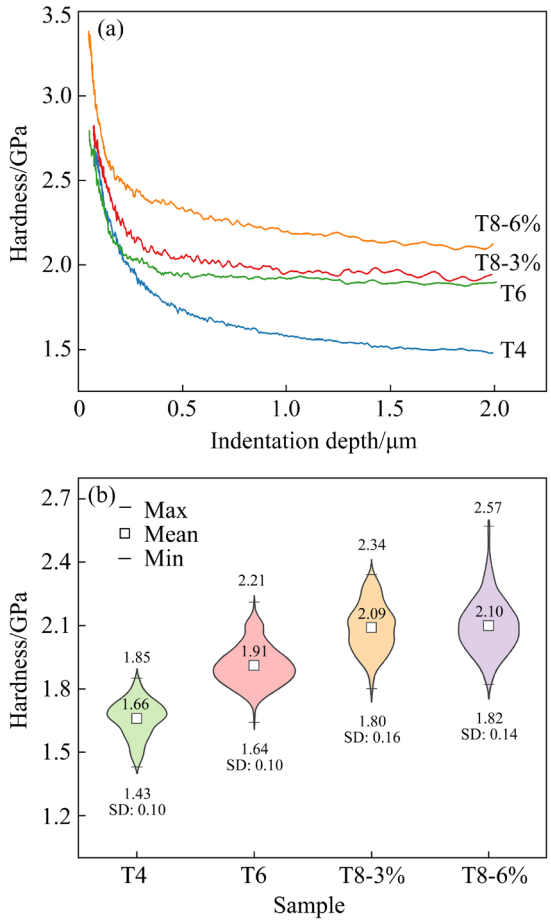

Fig. 6 Results of nanoindentation test: (a) Hardness−indentation depth curves for different samples; (b) Average hardness and hardness distribution for different samples

Figure 6(b) illustrates the average hardness and its distribution for the AA2099 Al−Li alloy subjected to various heat treatments. These treatments significantly affect the mechanical performance of the alloy. The results demonstrate a rise in hardness, correlating with an increase in the precipitate density of the main strength phase, i.e., T_1 (Fig. 3). In addition, the standard deviation (SD) in hardness for the T8 samples is observed to be higher compared to that for the T4 and T6 samples. This variation is likely due to the increased inhomogeneity in the T_1 phases or the dislocation structures caused by pre-stretching [33]. Figure 7 shows the tensile curves of AA2099 Al−Li alloy with various heat treatments. Consistent with the findings from hardness measurements, the yield strength of the alloy demonstrates significant enhancement subsequent to various heat treatments.

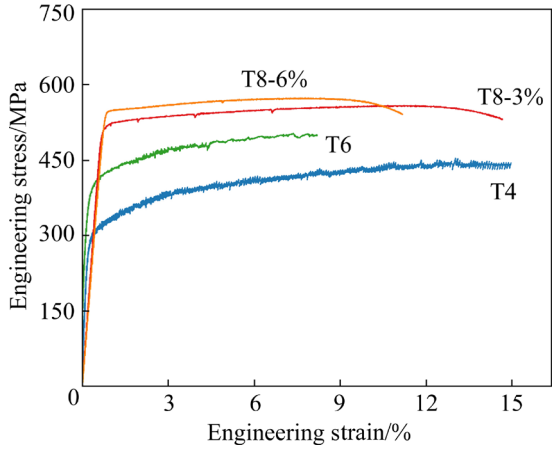

Fig. 7 Engineering stress−strain curves of samples after different heat treatments

3.3 Feature importance ranking on hardness

The RFR algorithm was employed to predict the hardness of various samples. This process involved an iterative adjustment phase, which included the integration of new data and parameter tuning, with the aim of refining the machine learning model and improving its predictive performance. The final predicted hardness values for different samples are depicted in Fig. 8. The R^2 values obtained for hardness are 0.73, 0.66, 0.74, and 0.68 for the T4, T6, T8-3%, and T8-6% samples, respectively. The R^2 value serves as a measure of the success of prediction by quantifying the deviation between the predicted and actual values. A larger R^2 value indicates a smaller deviation, indicating a more accurate prediction. Therefore, the prediction accuracy can be evaluated using the R^2 value, where a value above 0.6 is considered indicative of a reliable prediction.

The utilization of the RFR algorithm facilitates the exploration of feature importance, helping to identify the input variables with the greatest influence on hardness prediction. As shown in Fig. 9, the feature importance ranking reveals that

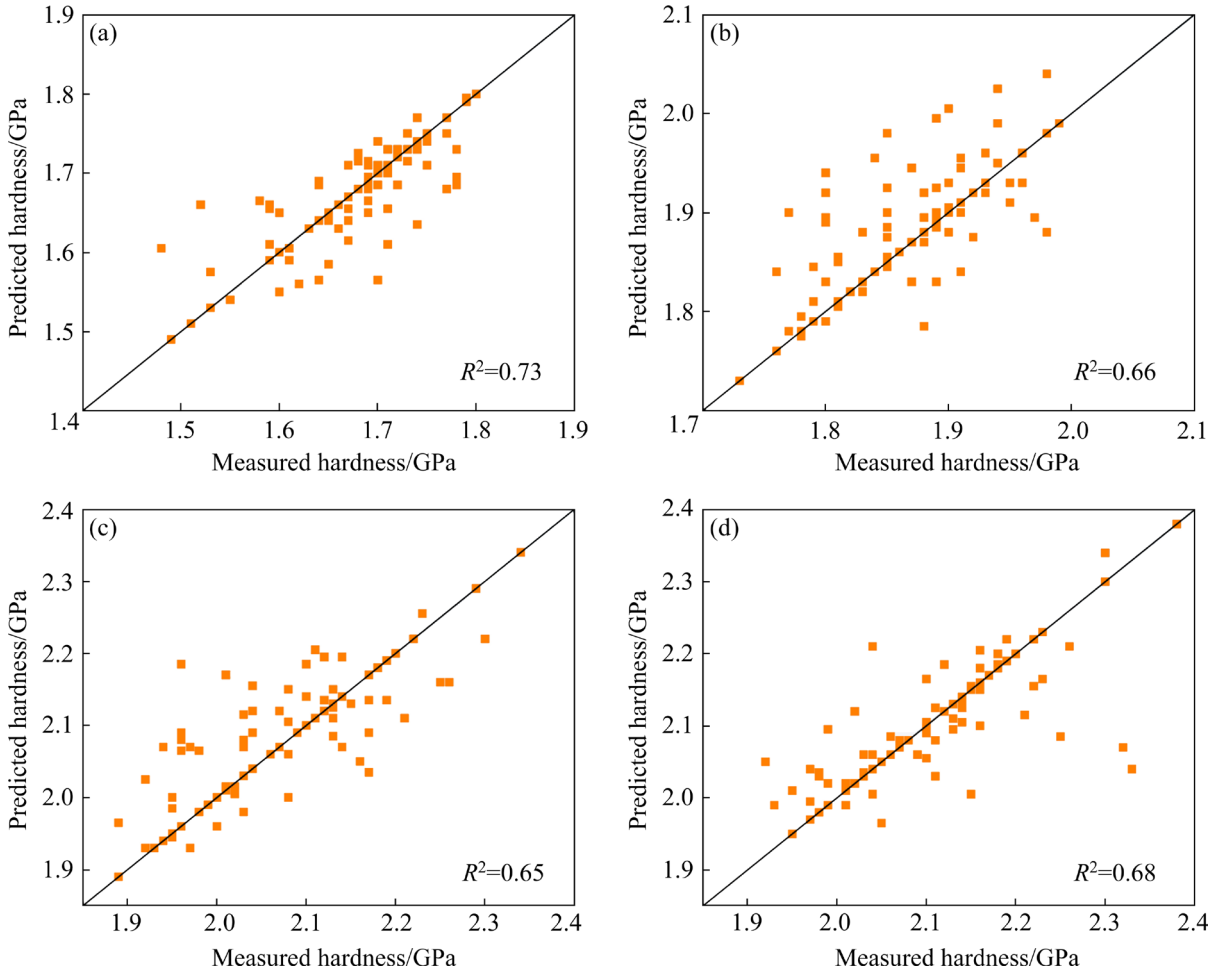

Fig. 8 Comparison of predicted hardness values obtained from RFR machine learning models with measured hardness values for different samples: (a) T4; (b) T6; (c) T8-3%; (d) T8-6%

geometric features (D_{dis} and D_{min}) have the most prominent impact on hardness of all samples. Additionally, for the T4 sample, SF_{FD} exhibits the second highest degree of influence, whereas $\sin\theta_{min}$ emerges as the second most influential factor for the T8-3% and T8-6% samples. Notably, among the evaluated feature variables (SF_{FD}, SF_{TD}, and SF_{ND}), SF_{FD} is identified as the most critical feature in determining hardness.

Considering exhaustively all the critical features influencing hardness remains a challenging topic of discussion. The absence of key features may potentially lead to suboptimal model performance, thereby diminishing the accuracy of hardness prediction. However, the comprehensive analysis presented in this study provides valuable insights into the underlying factors that contribute to the predicted hardness values across diverse sample variations.

4 Analysis and modeling

4.1 Deformed region around indents based on hybrid of machine learning and slip trace analysis

Figure 10 shows the indentation morphology and slip trace analysis results of the T4, T6 and T8-3% samples. Two sets of slip planes are activated on each side of the triangular impression in the T6 and T8-3% samples, while the activation of a single slip plane is more common on each side of the triangular impression in the T4 sample. This variation in deformation behaviors may be related to the slip modes of dislocations. In the T4 sample, cluster strengthening predominates with strong planar slip [34], resulting in the activation of a single slip plane. In contrast, in the artificially aged sample (T6 and T8-3%), a large number of

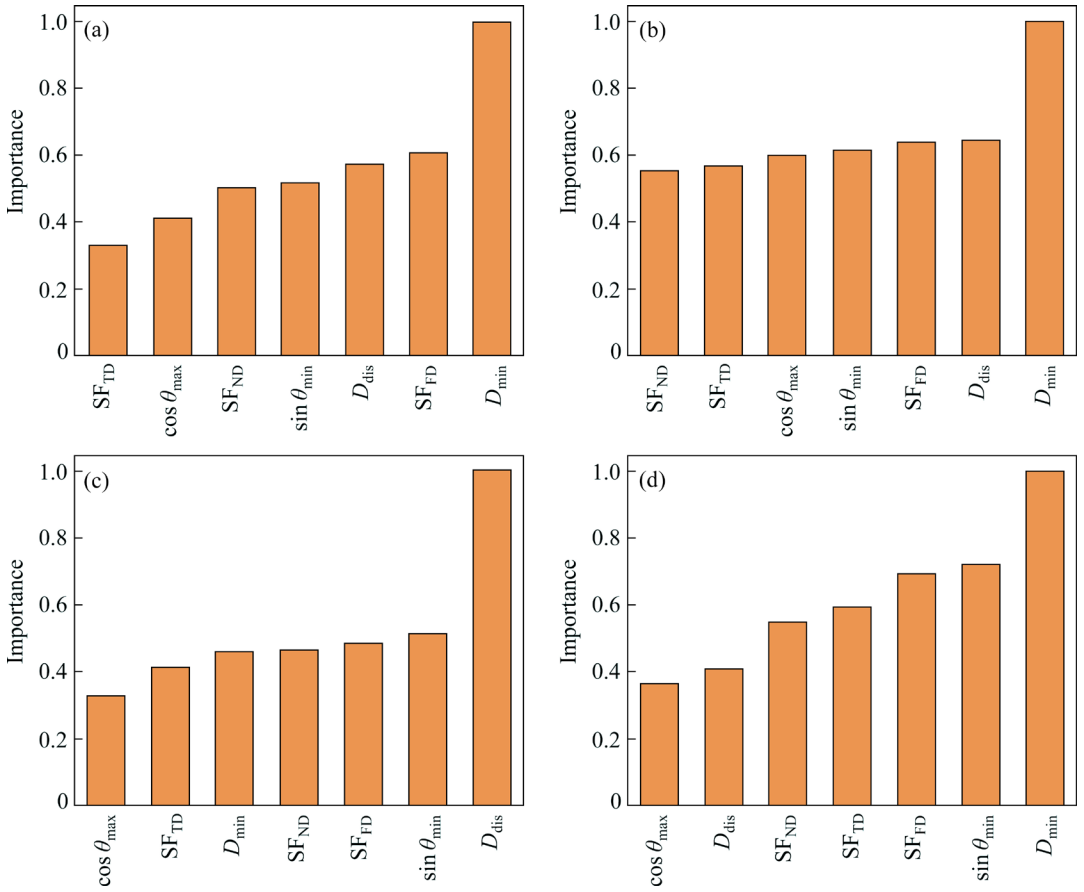

Fig. 9 Feature importance ranking of AA2099 Al−Li alloy after different heat treatments: (a) T4; (b) T6; (c) T8-3%; (d) T8-6%

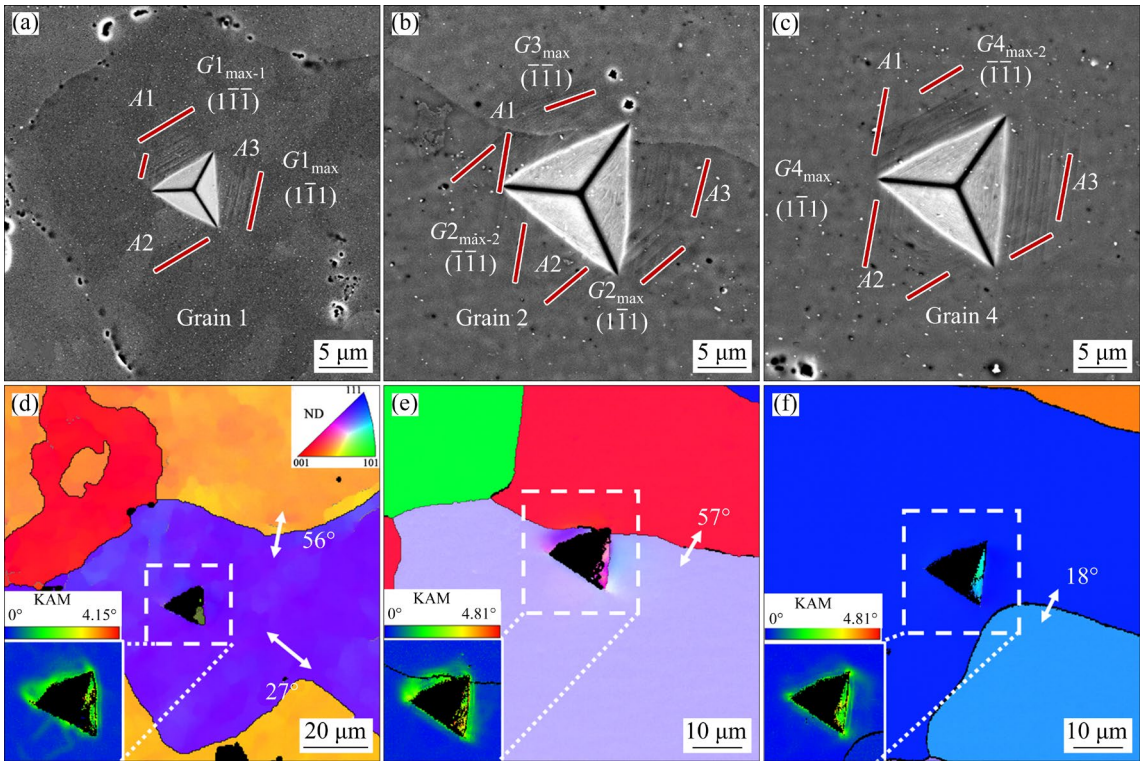

Fig. 10 Indentation morphologies (a−c) and slip trace analysis results (d−f) of samples: (a, d) T4; (b, e) T6; (c, f) T8-3%

precipitates suppress planar slip behaviors, leading to the activation of more slip systems to coordinate deformation.

Slip traces are pivotal in elucidating the micro-mechanisms of plastic deformation. Active slip systems often exhibit higher Schmidt factors, which depend on the orientation of the slip system relative to the applied stress. To determine the Schmidt factor, the direction of applied stress in the crystal coordinate system is essential. Machine learning results suggest that the hardness is most strongly correlated with SF_{FD} when the stress is applied along the FD. Therefore, for Schmidt factor calculations on the contact planes $A1$, $A2$, and $A3$ of the indenter tip (as shown in Fig. 10(a−c)), the stress direction is assumed to be parallel to the direction of indentation.

Figures 10(d−f) present IPF maps of the corresponding areas around the indentation, showcasing the crystal orientations of grains surrounding the indentation. EBSD data analysis indicates that the two activated slip systems in the T4 sample (Fig. 10(a)) are located on the $(1\bar{1}1)$ and $(1\bar{1}\bar{1})$ slip planes of Grain 1, respectively. These slip systems correspond to the Schmidt factors with the highest ($G1_{max}$) or the next highest ($G1_{max\text{-}1}$) values when the loading direction is assumed to be along the FD. In the T6 sample (Fig. 10(b)), the indentation is located near the grain boundary. The two activated slip systems of Grain 2 are located on the $(\bar{1}\bar{1}1)$ and $(1\bar{1}1)$ slip planes, respectively. These slip systems correspond to the Schmidt factors with the highest ($G2_{max}$) or third highest ($G2_{max\text{-}2}$) values. The single activated slip systems of Grain 3 are located on the $(\bar{1}\bar{1}1)$ slip planes, which correspond to the Schmidt factors with the highest ($G3_{max}$) values. In the T8-3% sample, the same result is obtained, with the two activated slip systems located on the $(1\bar{1}1)$ and $(1\bar{1}\bar{1})$ slip planes of Grain 4. These analysis results indicate that the deformation behavior near the indentation is predominantly influenced by the stress in the FD.

Analyzing the stress field of an indentation is challenging. Several studies [35−37] have employed finite element simulations for this purpose. In this study, machine learning models have been utilized, making various assumptions about the stress field surrounding the indentation. Specifically, the deformation behavior near the indentation is hypothesized to be primarily influenced by the stress applied in the FD, TD, and ND. We calculated the Schmid factors for the grain located at the indentation when subjected to stress in the FD, TD, and ND. SF_{FD} is identified as the most critical feature in determining hardness. In other words, the results from machine learning method also indicate that the deformation behavior near the indentation is predominantly influenced by the stress applied in the FD. The stress field surrounding the indentation can be likened to that of uniaxial compression in the FD.

Figures 10(d−f) highlight the high strain regions with kernel average misorientation (KAM) maps. The estimation of geometrically necessary dislocations (GND) is based on KAM. In the T6 sample, an interesting observation is the visible accumulation of GND near the grain boundary in the vicinity of $A1$. This accumulation indicates a strong hindering effect of high-angle grain boundaries on dislocation slip, which leads to an increase in hardness [38,39]. In contrast, in the T8-3% sample, there is no significant pileup of dislocations near the grain boundaries in the vicinity of $A2$ and $A3$. This could be attributed to the lower misorientations of these boundaries, which have less impact on plastic deformation, especially near low-angle grain boundaries. This finding is consistent with the analysis of important distribution results in machine learning, where grain boundaries are identified as one of the key factors affecting the hardness.

The geometric feature parameters D_{dis} and D_{min} are listed as the most important features in the analysis of important distribution results in machine learning. During model training, it was found that the feature importance distribution of these two parameters differs significantly among different samples. Notably, these two parameters exhibit a positive correlation and strong association. Typically, a reduction in grain size leads to a decrease in the nearest distance between the indentation and the grain boundary. Interestingly, both parameters have similar effects on the hardness, as evidenced by the pileup of dislocations at grain boundaries. Using a single parameter feature seems to result in unstable feature importance distribution. Therefore, if both parameters need to be considered at the same time, it is recommended to multiply them to create a

composite feature, which can significantly enhance the predictive ability of the machine learning model. In this study, however, we opted to simply superimpose the importance of these two parameters.

EBSD data analysis, combined with machine learning, revealed that crystallographic orientation exerts a significant influence on hardness, which is further exacerbated by the presence of T_1 phases. Due to the precipitation of T_1 phases along $\{111\}_{Al}$ habit planes, four crystal orientation variants correspond to different non-parallel $(111)_{Al}$ planes. Figure 11 illustrates diagrams representing the four variants of T_1 phases in relation to specific indentation loading directions. In the fiber texture ⟨111⟩//TD (Fig. 11(a)), the indenter encounters obstructions from two inclined T_1 variants and two vertically parallel T_1 phase variants. In contrast, for the fiber texture ⟨111⟩//FD (Fig. 11(b)), the indenter faces obstructions from one vertical T_1 variant and three inclined T_1 variants. The T_1 phase variants precipitate along different $\{111\}_{Al}$ habit planes in grains with different crystal orientations, which may lead to different amounts of inclined/face-on T_1 phase variants during FD loading. These T_1 phase variants, with their different angles relative to the surface plane, exhibit different resistances to indenter loading [40]. Consequently, $\sin\theta_{min}$ emerges as the second most influential factor affecting hardness of the T8-3% and T8-6% samples, which contain a substantial amount of lamellar T_1 phases.

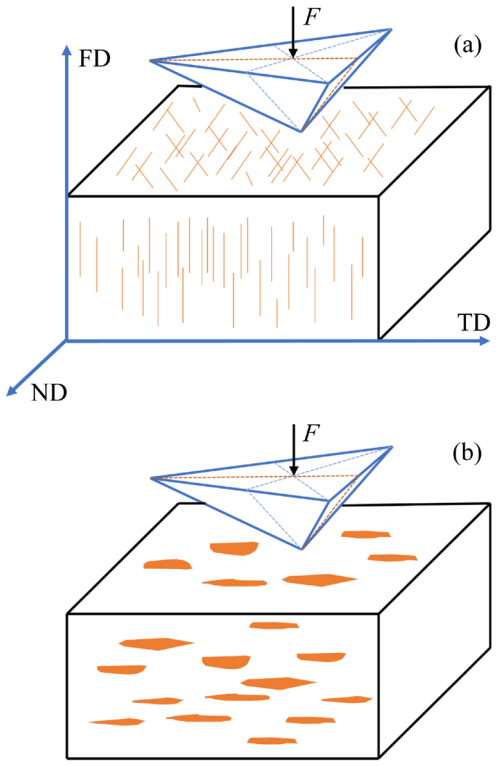

Fig. 11 Schematic diagrams of T_1 phase orientation variants with respect to specific indentation loading in different crystal orientations: (a) ⟨111⟩//TD; (b) ⟨111⟩//FD

4.2 Strength modeling

4.2.1 Yield strength modeling

Various models have established to show a relationship between the critical resolved shear stress (τ) and the yield strength (σ_y) of polycrystalline metals [41,42]. The yield strength of the alloys can be approximately described by the following relationship [43−45]:

$$\sigma_y=M\tau=M(\tau_b+\Delta\tau_p+\Delta\tau_\rho) \quad (4)$$

where M is the Taylor factor (~3.1). M^{-1} is the Schmidt factor (SF_{FD}) for a monocrystal. τ_b is the base strength, $\Delta\tau_p$ and $\Delta\tau_\rho$ are the increase in strength due to precipitation and dislocation density, respectively. It is assumed that the increase in strength due to solid solution hardening will remain constant during artificial aging as any change from a loss of solid solution strengthening is relatively small compared to the significant strength gains from strain and precipitation hardening. Therefore, the yield strength of the annealed 2099 Al−Li alloy, tested immediately after solution treatment, was used to determine the base strength τ_b.

The measured dislocation density values obtained by XRD of the material following stretching in the T3 temper can be used to estimate the contribution from forest hardening to the CRSS of the alloy. The standard expression relating dislocation density to the CRSS is given by [46]

$$\Delta\tau_\rho=\alpha Gb\rho^{1/2} \quad (5)$$

where α is a dimensionless constant between 0.2 and 0.5, and G is the shear modulus.

The increase in strength resulting from precipitation or clusters in the sample can be quantified as the total yield strength minus the base strength and strain hardening contribution. Several main strength contributions can be separated based on the above calculation results, as shown in Fig. 12.

4.2.2 Hardness modeling

The correlation between hardness (H) and

yield strength can be expressed as [47−49]

$$H=a_1\sigma_y+b_1 \quad (6)$$

where a_1 and b_1 are constants that depend on the indentation displacement, with their values approaching 1.907 and 1.079 GPa, respectively. The hardness−yield strength relationship is presented in Fig. 13, exhibiting a strong alignment with the ideal linear behavior.

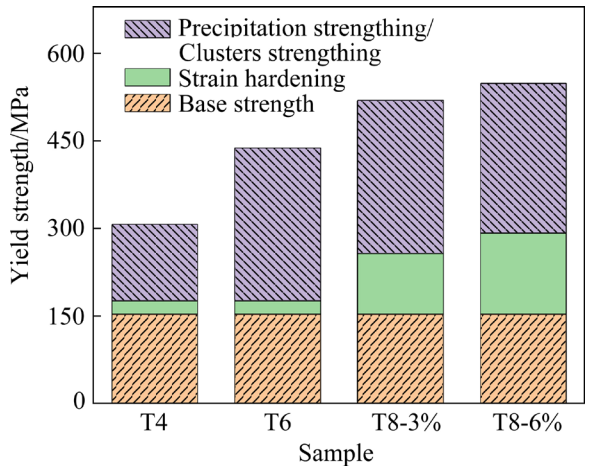

Fig. 12 Main strengthening terms of AA2099 Al−Li alloy after different heat treatments

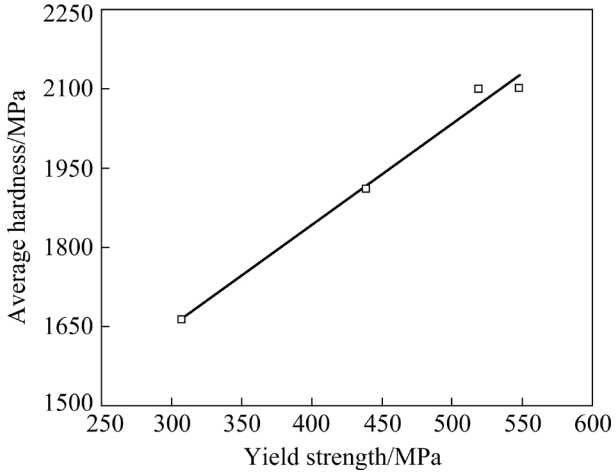

Fig. 13 Change in average hardness with yield strength

According to Eq. (4), we can get the following relationship:

$$H=a_1M\tau+b_1 \quad (7)$$

Within the same sample, notable variations in hardness are observed due to microstructural heterogeneity. The results of machine learning and plastic deformation of indentation indicate that high-angle grain boundaries strongly impede dislocation slip, resulting in increased hardness. Previous investigations [50,51] have demonstrated that the hardening effect intensifies as the distance from the indentations to the grain boundary D_{dis} decreases. This distance can be interpreted as the length of dislocation pileup [52]. Therefore, it is clear that an additional parameter, namely D_{dis}, is required to describe such deviation in hardness among different grains, as it significantly affects the hardness. The influence of grain boundaries on shear stress can be expressed in the following form [53,54]:

$$\tau=\tau_0+k_0d^{-1/2} \quad (8)$$

where τ_0 is the friction stress, k_0 is a constant, and d is the grain diameter or D_{dis}. Then, the hardness can be expressed as

$$H=a_2M\tau(1+kd^{-1/2})+b_2 \quad (9)$$

where a_2 and b_2 are constants, and k is a synergistic strengthening constant, approaching a value of 1 μm$^{-1/2}$. As depicted in Fig. 14(a), the hardness of the T4 sample, calculated using Eq. (9), aligns reasonably well with the experimentally determined hardness. However, when D_{dis} is lower than 20 μm, the discrepancy between the predicted hardness in the model and the experimentally measured hardness becomes more pronounced. This may be due to the insufficient accuracy in measuring D_{dis} or the fact that the hardness is also influenced by the crystal orientation of the adjacent grains [50].

However, this model fails to consider the impact of precipitate morphology on hardness. In the T8 temper, the sine value of the angle between the {111} slip plane and the surface plane is more important than the Schmidt factor for predicting hardness. The indenter encounters varying resistance from different T_1 phase variants, resulting in different CRSS for different grains. The hardness is fitted with $\sin\theta_{min}$ (Fig. 14(b)), using the relationship:

$$H=a_3M\tau(1+kd^{-1/2}+c\sin\theta_{min})+b_3 \quad (10)$$

where a_3 and b_3 constants, and c is also a constant, with a fitted value of c=0.9. The results reveal a near-linear increase in hardness with increasing $\sin\theta_{min}$. It is worth noting that disparities in the c values are potentially observable for the T8-6% sample owing to heterogeneities in the dimensions and the number density of precipitates.

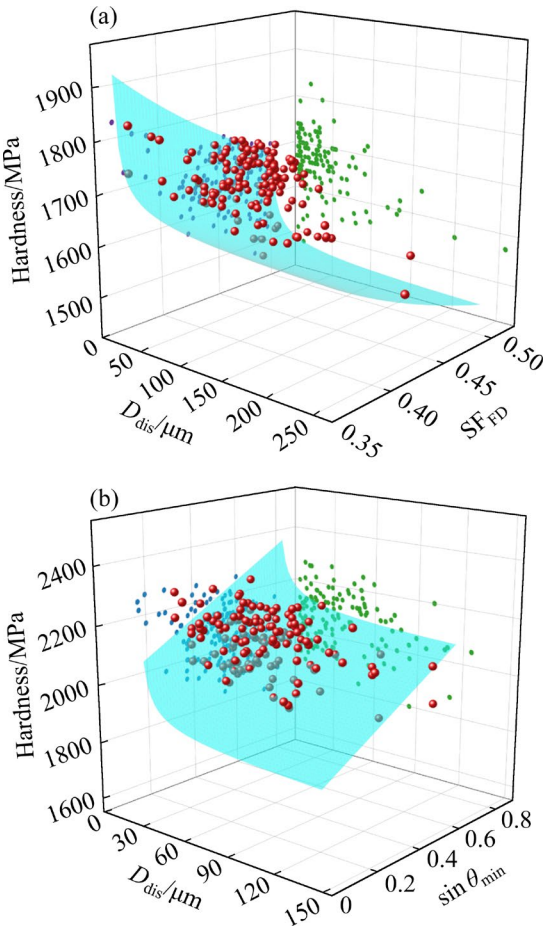

Fig. 14 Hardness as function of D_{dis} and SF_{FD} in T4 sample (a), and D_{dis} and sin θ_{min} in T8-3% sample (b)

5 Conclusions

(1) Geometric feature parameters (D_{dis} and D_{min}) emerge as crucial determinants in hardness prediction. High-angle grain boundaries stall dislocation slip, leading to dislocation pileup and subsequent hardness increase. Conversely, low-angle grain boundaries do not exhibit this hardening effect.

(2) A lower SF_{FD} and a higher sin θ_{min} are correlated with the increased hardness. This indicates the significant impact of crystallographic orientation on the hardness, an effect that is further amplified by the presence of T_1 phases along $\{111\}_{Al}$ habit planes. This variation in hardness can be attributed to different T_1 variants, of which the indenter encounters during loading.

(3) The importance of these features varies depending on the presence of T_1 phases. In samples without a significant amount of T_1 phases (T4 and T6 samples), the feature importance ranking is D_{dis} or D_{min}> SF_{FD} > sin θ_{min}. However, in samples with a large amount of T_1 phases (T8-3% and T8-6% samples), the ranking shifts to D_{dis} or D_{min} > sin θ_{min} > SF_{FD}.

CRediT authorship contribution statement

Xiang-hui ZHU: Conceptualization, Methodology, Software, Data curation, Writing − Original draft; **Xu-sheng YANG:** Investigation, Methodology, Writing − Review & editing; **Wei-jiu HUANG:** Conceptualization, Project administration, Supervision, Funding acquisition, Writing − Review & editing; **Miao GONG:** Data curation, Software; **Xin WANG** and **Meng-di LI:** Data curation.

Declaration of competing interest

The authors declare that they have no known competing financial interests or personal relationships that could have appeared to influence the work reported in this paper.

Acknowledgments

This work was financially supported by the National Natural Science Foundation of China (No. 51871038), and the Natural Science Foundation of Chongqing, China (Nos. CSTB2022NSCQ-LZX0002, cstc2021jcyj-msxmX0960).

References

[1] PENG Peng, SU Jian, HE Qing-song, CHEN Rui-nan, CHAI Sen-sen, YU Da-liang, DAI Qing-wei, LU Jian. Solid-state bonding process induced highly synergistic mechanical properties of 6061 Al alloy joint by shear deformation [J]. Journal of Materials Science & Technology, 2023, 164: 168−178.

[2] WANG Sen, LV Bin-jiang, XU Tie-wei, CUI Ning, GUO Feng. Relationship between microstructure and mechanical properties of as-extruded and peak-aged Mg−6Al−3Sn−2Zn alloys [J]. Transactions of Nonferrous Metals Society of China, 2023, 33(5): 1385−1397.

[3] WANG Xiao-feng, GUO Ming-xing, PENG Wen-fei, WANG Yong-gang, ZHUANG Lin-zhong. Relationship among solution heating rate, mechanical properties, microstructure and texture of Al−Mg−Si−Cu alloy [J]. Transactions of Nonferrous Metals Society of China, 2021, 31(1): 36−52.

[4] DORIN T, DESCHAMPS A, GEUSER F D, SIGLI C. Quantification and modelling of the microstructure/strength relationship by tailoring the morphological parameters of the T_1 phase in an Al−Cu−Li alloy [J]. Acta Materialia, 2014, 75: 134−146.

[5] YANG Xu-sheng, HUANG Wei-jiu, ZHU Xiang-hui, GUO

Fei, HU Li, ZHANG Ran. The effects of precipitates on microstructure and β-fiber texture in an Al−Cu−Li alloy during hot rolling [J]. Materials Characterization, 2020, 162: 110186.

[6] YANG Xu-sheng, CHAI Lin-jiang, HUANG Wei-jiu, MA Yan-long, ZHANG Zhen-hao. Texture evolution and microstructural thermal stability of as-extruded AA2099 during hot deformation [J]. Materials Science and Engineering A, 2016, 675: 431−436.

[7] LIN Yi, ZHENG Zi-qiao, ZHANG Hai-feng, HAN Ye. Effect of heat treatment process on tensile properties of 2A97 Al−Li alloy: Experiment and BP neural network simulation [J]. Transactions of Nonferrous Metals Society of China, 2013, 23(6): 1728−1736.

[8] LU Ding-ding, WANG Gui, LI Jin-feng, DENG San-xi, HUANG Yang, XIANG Hui, YAO Yong, MA Peng-cheng, CHEN Yong-lai, ZHANG Xu-hu. Effect of grain structure and precipitate on tensile properties and low-cycle fatigue behaviors of 2A55 Al−Cu−Li alloy [J]. International Journal of Fatigue, 2022, 159: 106834.

[9] WEN Feng, CHEN Ji-qiang, HAN Shuang, ZHOU Zi-xiang, ZHONG Shi-biao, ZHANG Ying-hui, LI Wei-rong, GUAN Ren-guo. Effect of crystal orientations and precipitates on corrosion behavior of Al−Cu−Li single crystals [J]. Transactions of Nonferrous Metals Society of China, 2022, 32(12): 3887−3900.

[10] LU Ding-ding, LI Jin-feng, NING Hong, MA Peng-cheng, CHEN Yong-lai, ZHANG Xu-hu, ZHANG Kai, LI Jian-mei, ZHANG Rui-feng. Effects of microstructure on tensile properties of AA2050-T84 Al−Li alloy [J]. Transactions of Nonferrous Metals Society of China, 2021, 31(5): 1189−1204.

[11] WANG Ming-zhi, WU Jian-jun, ZHAN Xue-peng, GUO Rui-chao, HUI Yu, FAN He. On the determination of the anisotropic plasticity of metal materials by using instrumented indentation [J]. Materials & Design, 2016, 111: 98−107.

[12] CSANÁDI T, BLANDA M, CHINH N Q, HVIZDOŠ P, DUSZA J. Orientation-dependent hardness and nano-indentation-induced deformation mechanisms of WC crystals [J]. Acta Materialia, 2015, 83: 397−407.

[13] BARDEL D, PEREZ M, NELIAS D, DESCHAMPS A, HUTCHINSON C R, MAISONNETTE D, CHAISE T, GARNIER J, BOURLIER F. Coupled precipitation and yield strength modelling for non-isothermal treatments of a 6061 aluminium alloy [J]. Acta Materialia, 2014, 62: 129−140.

[14] YANG Ming-jun, OREKHOV A, HU Zhi-yi, FENG Man, JIN Shen-bao, SHA Gang, LI Kai, SAMAEE V, SONG Min, DU Yong, TENDELOO G, SCHRYVERS D. Shearing and rotation of β'' and β' precipitates in an Al−Mg−Si alloy under tensile deformation: In-situ and ex-situ studies [J]. Acta Materialia, 2021, 220: 117310.

[15] SANTOS-GÜEMES R, BELLÓN B, ESTEBAN-MANZANARES G, SEGURADO J, CAPOLUNGO L, LLORCA J. Multiscale modelling of precipitation hardening in Al−Cu alloys: Dislocation dynamics simulations and experimental validation [J]. Acta Materialia, 2020, 188: 475−485.

[16] LIU Yan-fang, CAO Yang, MAO Qing-zhong, ZHOU Hao, ZHAO Yong-hao, JIANG Wei, LIU Ying, WANG Jing-tao, YOU Ze-sheng, ZHU Yun-tian. Critical microstructures and defects in heterostructured materials and their effects on mechanical properties [J]. Acta Materialia, 2020, 189: 129−144.

[17] DURODOLA J F. Machine learning for design, phase transformation and mechanical properties of alloys [J]. Progress in Materials Science, 2022, 123: 100797.

[18] LIU Yue, GUO Bi-ru, ZOU Xin-xin, LI Ya-jie, SHI Si-qi. Machine learning assisted materials design and discovery for rechargeable batteries [J]. Energy Storage Materials, 2020, 31: 434−450.

[19] LIU Yue, ZHAO Tian-lu, JU Wang-wei, SHI Si-qi. Materials discovery and design using machine learning [J]. Journal of Materiomics, 2017, 3(3): 159−177.

[20] MANGAL A, HOLM E A. Applied machine learning to predict stress hotspots I: Face centered cubic materials [J]. International Journal of Plasticity, 2018, 111: 122−134.

[21] HART G L, MUELLER T, TOHER C, CURTAROLO S. Machine learning for alloys [J]. Nature Reviews Materials, 2021, 6(8): 730−755.

[22] FADAEIFARD F, MATORI K A, GARAVI F, AL-FALAHI M, SARRIGANI G V. Effect of post weld heat treatment on microstructure and mechanical properties of gas tungsten arc welded AA6061-T6 alloy [J]. Transactions of Nonferrous Metals Society of China, 2016, 26(12): 3102−3114.

[23] SCHUH C A. Nanoindentation studies of materials [J]. Materials Today, 2006, 9(5): 32−40.

[24] LIU Yue, YANG Zheng-wei, ZOU Xin-xin, MA Shu-chang, LIU Da-hui, AVDEEV M, SHI Si-qi. Data quantity governance for machine learning in materials science [J]. National Science Review, 2023, 10(7): 125.

[25] BREIMAN L. Random forest [J]. Machine Learning, 2001, 45: 5−32.

[26] DECREUS B, DESCHAMPS A, GEUSER F, DONNADIEU P, SIGLI C, WEYLAND M. The influence of Cu/Li ratio on precipitation in Al−Cu−Li−x alloys [J]. Acta Materialia, 2013, 61(6): 2207−2218.

[27] RODGERS B I, PRANGNELL P B. Quantification of the influence of increased pre-stretching on microstructure−strength relationships in the Al−Cu−Li alloy AA2195 [J]. Acta Materialia, 2016, 108: 55−67.

[28] UNGÁR T. Microstructural parameters from X-ray diffraction peak broadening [J]. Scripta Materialia, 2004, 51(8): 777−781.

[29] UNGÁR T. Dislocation densities, arrangements and character from X-ray diffraction experiments [J]. Materials Science and Engineering A, 2001, 309/310: 14−22.

[30] WOO W, UNGÁR T, FENG Z L, KENIK E, CLAUSEN B. X-ray and neutron diffraction measurements of dislocation density and subgrain size in a friction-stir-welded aluminum alloy [J]. Metallurgical and Materials Transactions A, 2010, 41: 1210−1216.

[31] UNGÁR T, GUBICZA J, RIBÁRIK G, BORBÉLY A. Crystallite size distribution and dislocation structure determined by diffraction profile analysis: Principles and practical application to cubic and hexagonal crystals [J]. Journal of Applied Crystallography, 2001, 34(3): 298−310.

[32] BORBÉLY A, DRAGOMIR-CERNATESCU J, RIBÁRIK G, UNGÁR T. Computer program ANIZC for the calculation of diffraction contrast factors of dislocations in elastically anisotropic cubic, hexagonal and trigonal crystals [J]. Journal of Applied Crystallography, 2003, 36(1): 160−162.

[33] ZHU Xiang-hui, YANG Xu-sheng, HUANG Wei-jiu, QIU Wei-yi, WANG Xin, GUO Fei, HU Li, GONG Miao. Influence of pre-stretching on the tensile strength, fatigue properties and the in-plane anisotropy in Al−Cu−Li alloy AA2099 [J]. Journal of Materials Science & Technology, 2023, 145: 249−259.

[34] MA Pei-pei, LIU Chun-hui, CHEN Qiu-yu, WANG Qing, ZHAN Li-hua, LI Jian-jun. Natural-ageing-enhanced precipitation near grain boundaries in high-strength aluminum alloy [J]. Journal of Materials Science & Technology, 2020, 46: 107−113.

[35] BHOWMIK A, LEE J, BRITTON T B, LIU W J, JUN T S, SERNICOLA G, KARIMPOUR M, BALINT D S, GIULIANI F. Deformation behaviour of [001] oriented MgO using combined in-situ nano-indentation and micro-Laue diffraction [J]. Acta Materialia, 2018, 145: 516−531.

[36] SU Y, ZAMBALDI C, MERCIER D, EISENLOHR P, BIELER T R, CRIMP M A. Quantifying deformation processes near grain boundaries in α titanium using nanoindentation and crystal plasticity modeling [J]. International Journal of Plasticity, 2016, 86: 170−186.

[37] LIU M, LU C, TIEU K A, PENG C T, KONG C. A combined experimental-numerical approach for determining mechanical properties of aluminum subjects to nanoindentation [J]. Scientific Reports, 2015, 5: 15072.

[38] MILMAN Y V, GOLUBENKO A A, DUB S N. Indentation size effect in nanohardness [J]. Acta Materialia, 2011, 59(20): 7480−7487.

[39] SOER W A, HOSSON J T M. Detection of grain-boundary resistance to slip transfer using nanoindentation [J]. Materials Letters, 2005, 59(24/25): 3192−3195.

[40] DUAN Shu-wei, GUO Fu-qiang, ZHANG Yong-gang, CHONG Kai, LEE S, MATSUDA K, ZOU Yong. Effects of texture and precipitates characteristics on anisotropic hardness evolution during artificial aging for an Al−Cu−Li alloy [J]. Materials & Design, 2021, 212: 110216.

[41] GHOSH M, MIROUX A, KESTENS L A I. Experimental study and modelling of the role of solutes, precipitates and temperature on the work-hardening of AA6xxx aluminium alloys [J]. Materials Science and Engineering A, 2021, 805: 140615.

[42] VAUCORBEIL A, POOLE W J, SINCLAIR C W. The superposition of strengthening contributions in engineering alloys [J]. Materials Science and Engineering A, 2013, 582: 147−154.

[43] STARINK M J, WANG S C. A model for the yield strength of overaged Al−Zn−Mg−Cu alloys [J]. Acta Materialia, 2003, 51(17): 5131−5150.

[44] MYHR O R, GRONG Ø, ANDERSEN S J. Modelling of the age hardening behaviour of Al−Mg−Si alloys [J]. Acta Materialia, 2001, 49(1): 65−75.

[45] CLAUSEN B, LORENTZEN T, LEFFERS T. Self-consistent modelling of the plastic deformation of FCC polycrystals and its implications for diffraction measurements of internal stresses [J]. Acta Materialia, 1998, 46(9): 3087−3098.

[46] MADEC R, DEVINCRE B, KUBIN L P. From dislocation junctions to forest hardening [J]. Physical Review Letters, 2002, 89(25): 255508.

[47] TAO Ping, GONG Jian-ming, WANG Yan-fei, JIANG Yong, LI Yang, CEN Wei-wei. Characterization on stress-strain behavior of ferrite and austenite in a 2205 duplex stainless steel based on nanoindentation and finite element method [J]. Results in Physics, 2018, 11: 377−384.

[48] CURLE U A, CORNISH L A, GOVENDER G. Predicting yield strengths of Al−Zn−Mg−Cu−(Zr) aluminium alloys based on alloy composition or hardness [J]. Materials & Design, 2016, 99: 211−218.

[49] RODRÍGUEZ R, GUTIERREZ I. Correlation between nanoindentation and tensile properties: Influence of the indentation size effect [J]. Materials Science and Engineering: A, 2003, 361(1): 377−384.

[50] VACHHANI S J, DOHERTY R D, KALIDINDI S R. Studies of grain boundary regions in deformed polycrystalline aluminum using spherical nanoindentation [J]. International Journal of Plasticity, 2016, 81: 87−101.

[51] VOYIADJIS G Z, ZHANG C. The mechanical behavior during nanoindentation near the grain boundary in a bicrystal FCC metal [J]. Materials Science and Engineering A, 2015, 621: 218−228.

[52] FAGHIHI D, VOYIADJIS G Z. Determination of nanoindentation size effects and variable material intrinsic length scale for body-centered cubic metals [J]. Mechanics of Materials, 2012, 44: 189−211.

[53] MEYERS M A, CHAWLA K K. Mechanical behavior of materials [M]. Cambridge, UK: Cambridge University Press, 2008.

[54] ESHELBY J D, FRANK F C, NABARRO F. The equilibrium of linear arrays of dislocations. [J]. The London, Edinburgh, and Dublin Philosophical Magazine and Journal of Science, 1951, 42(327): 351−364.

基于机器学习与显微组织的 AA2099 铝锂合金显微组织与硬度关系建模

祝祥辉[1,2]，杨绪盛[2]，黄伟九[1,2]，龚 苗[3]，汪 鑫[1]，李梦迪[4]

1. 昆明理工大学 材料科学与工程学院，昆明 650093；
2. 重庆文理学院 材料科学与工程学院，重庆 402160；
3. 重庆理工大学 材料科学与工程学院，重庆 400044；
4. 重庆大学 材料科学与工程学院，重庆 400044

摘 要：提出一种将机器学习和显微组织分析相结合的方法，通过纳米压痕、X 射线衍射和电子背散射衍射(EBSD)技术，研究 AA2099 铝锂合金显微组织与硬度的关系。利用随机森林回归(RFR)模型，基于显微组织特征对硬度进行预测，揭示硬度的影响因素并对其重要性进行排序。研究表明，压痕到晶界的距离(D_{dis})越小、最短晶粒轴(D_{min})越短、Schmidt 因子(SF_{FD})越小以及{111}滑移面和表面夹角的正弦值($\sin\theta_{min}$)越大，硬度越高。在硬度预测中，D_{dis} 和 D_{min} 为关键因素。大角度晶界能阻碍位错滑移，从而提高材料硬度。此外，晶体学取向对硬度也具有显著影响，特别是在$\{111\}_{Al}$ 惯习面上析出 T_1 相时。这种影响归因于在压痕加载过程中所遇到的不同类型的 T_1 相变体。因此，显微组织特征的重要性排序取决于 T_1 相，在 T_1 相有限的样品中，排序为 D_{dis} 或 $D_{min} > SF_{FD} > \sin\theta_{min}$；而在具有大量 T_1 相的样品中，排序变为 D_{dis} 或 $D_{min} > \sin\theta_{min} > SF_{FD}$。

关键词：机器学习；T_1 相；硬度；铝锂合金

(Edited by Wei-ping CHEN)